Millimeter-wave emission characteristics of bilayer radar-infrared compound stealth material

Yayun Cheng (程亚运)[1,2], Fei Hu (胡 飞)[1,2], Feng He (贺 锋)[1,2,*], Liang Wu (吴 量)[1,2], and Xiaoqin He (何小琴)[1,2]

[1]*School of EIC, Huazhong University of Science and Technology, Wuhan 430074, China*
[2]*National Key Laboratory of Science and Technology on Multi-Spectral Information Processing, Wuhan 430074, China*
**Corresponding author: hefeng@hust.edu.cn*

Received January 12, 2016; accepted April 15, 2016; posted online May 26, 2016

To achieve radar and infrared stealth, an infrared stealth layer is usually added to the radar absorbing material (RAM) of stealth aircraft. By analyzing the millimeter-wave (MMW) emissivities of three stealth materials, this Letter investigates the impact of the added infrared stealth layer on the originally "hot" MMW emission of RAM. The theoretical and measured results indicate that, compared with the monolayer RAM, the MMW emission of the bilayer material is still strong and its emissivity is reduced by 0.1–0.2 at almost every incident angle. The results partially demonstrate the feasibility of detecting stealth aircraft coated with this bilayer stealth material.

OCIS codes: 280.4991, 350.4010, 120.1880, 290.6815.
doi: 10.3788/COL201614.062802.

Passive millimeter-wave (PMMW) technology has been used for various applications in astronomy, remote sensing and security checks due to the millimeter wave (MMW) ability to penetrate fog, smoke, clothing, and sandy soil in both daytime and nighttime operations[1–5]. PMMW imaging systems can generate images through the passive detection of naturally emitting MMW radiation from substances. In recent years, researchers have used PMMW technology for military applications, including detecting aircrafts[6–9], especially stealth fighters due to the "hot" MMW emission of radar-absorbing materials (RAMs). Traditional stealth fighters generally have RAM on the surface[10]. RAM helps to decrease radar cross section (RCS) because of the high absorptivity at the radar waveband. According to Kirchhoff's law of thermal radiation[11], the emissivity of a given object is equal to its absorptivity under the local thermodynamic equilibrium. In other words, an aircraft coated with RAM usually has a high brightness temperature at the radar waveband, even the MMW band[10]. Hence, we can usually obtain a 100–200 K brightness temperature contrast between the aircraft and the "cold" sky background[8,9].

In general, the RAM layer usually also has a high infrared emittance, which increases the detection probability by infrared sensors[12]. To decrease the high infrared emittance from the hot RAM layer, advanced stealth material was invented by adding an additional layer with low infrared emittance on the RAM[13,14]. However, the added infrared stealth layer may affect the MMW emission of the compound stealth material. Although the RAM layer has a high MMW brightness temperature, that of the infrared stealth layer is unknown. Exploratory and experimental research on the MMW emission characteristics of bilayer radar-infrared compound stealth materials (BSM-RIs) is carried out in this Letter. This investigation is important for the feasibility analysis of detecting aerial stealth targets coated with BSM-RI by using MMW radiometers.

In our work, we select three kinds of materials: BSM-RI, as mentioned above, monolayer radar stealth material (MSM-R), and monolayer infrared stealth material (MSM-I) with low infrared emittance. As shown in Fig. 1, a typical BSM-RI is considered and each layer is isotropic and homogeneous. By adding an infrared stealth layer, the original three-layer structure becomes a four-layer medium structure. The MMW emissivity model of MSM-R has been reported in the published literature[8,15]. According to similar theories, the MMW emissivity model of BSM-RI is deduced by analyzing the interactions of electromagnetic waves in the layers[16]. The four layers of media are air, the infrared layer, the RAM layer, and metal, and they are called layer 0, layer 1, layer 2, and layer 3, respectively. ϵ_i and μ_i $(i = 0, 1, 2)$ are the permittivity and permeability of layer i. E_i and E_r represent the incident and reflected

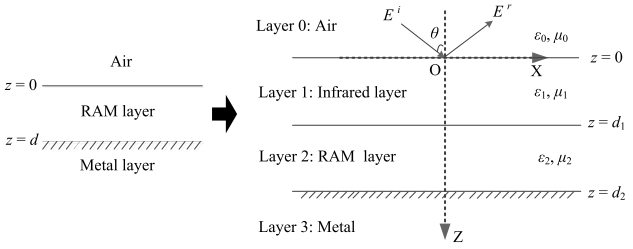

Fig. 1. Schematic of multilayer structure. The left and right ones are MSM-R and BSM-RI, respectively.

 © 2016 Chinese Optics Letters

electric fields, respectively. Assume a horizontally polarized incident electric field E_y of the form

$$\mathbf{E}^i = \hat{\mathbf{y}} E_y = \hat{\mathbf{y}} \exp[j\omega t - jk_0 \sin\theta + jk_0 z \cos\theta], \quad (1)$$

where θ is the incident angle, ω is the angular frequency, and k_0 is the wave number of free space. Then, the governing equation for the electric field in any layer is

$$\left(\frac{\partial^2}{\partial x^2} + \frac{\partial^2}{\partial z^2} + \omega^2 \mu\epsilon\right) E_y = 0. \quad (2)$$

Hence, with the time factor $e^{j\omega t}$ understood, the solution to Eq. (2) for the mth layer is

$$E_y = (A_m e^{jk_{zm}z} + B_m e^{-jk_{zm}z}) e^{-jk_0 x \sin\theta}, \quad (3)$$

$$k_{zm} = (\omega^2 \mu_m \epsilon_m - k_0^2 \sin^2\theta_0)^{1/2}, \quad (4)$$

where A_m and B_m are the unknown coefficients, and k_{zm} is the wave number of the mth layer in the z-axis direction. From Maxwell's equations, the corresponding magnetic fields are

$$H_{xm} = \frac{k_{zm}}{\omega\mu_m}(A_m e^{jk_{zm}z} - B_m e^{-jk_{zm}z}) e^{-jk_0 x \sin\theta}, \quad (5)$$

$$H_{zm} = \frac{k_0 \sin\theta}{\omega\mu_m}(A_m e^{jk_{zm}z} + B_m e^{-jk_{zm}z}) e^{-jk_0 x \sin\theta}. \quad (6)$$

According to the boundary conditions at $z = d_m$ (the continuity of the tangential electric field and the tangential magnetic field), we get

$$\begin{bmatrix} A_m e^{-jk_{zm}d_m} \\ B_m e^{jk_{zm}d_m} \end{bmatrix} = M_{m(m+1)} \begin{bmatrix} A_{m+1} e^{-jk_{z(m+1)}d_{m+1}} \\ B_{m+1} e^{jk_{z(m+1)}d_{m+1}} \end{bmatrix}. \quad (7)$$

The backward propagation matrix $M_{m(m-1)}$ is given by

$$M_{m(m+1)} = \frac{1}{2}\left(1 + \frac{\mu_m k_{z(m+1)}}{\mu_{m+1} k_{zm}}\right) \times \begin{bmatrix} e^{j\Theta} & R_{m(m+1)} e^{-j\Theta} \\ R_{m(m+1)} e^{j\Theta} & e^{-j\Theta} \end{bmatrix}, \quad (8)$$

$$R_{m(m+1)} = \frac{\mu_m k_{zm} - \mu_m k_{z(m+1)}}{\mu_m k_{zm} + \mu_m k_{z(m+1)}}, \quad (9)$$

$$\Theta = k_{z(m+1)}(d_{m+1} - d_m), \quad (10)$$

where $R_{m(m+1)}$ is the Fresnel reflection coefficient for horizontal polarization at the boundary $z = d_m$, and Θ is the phase shift. The field in the BSM-RI is a three-interface problem. At $z = 0$, the incident and the reflected field amplitudes are related to the transmitted field amplitudes by

$$\begin{bmatrix} 1 \\ R \end{bmatrix} = M_{01} M_{12} M_{23} \begin{bmatrix} T e^{-jk_{z3}d_3} \\ 0 \end{bmatrix}, \quad (11)$$

where R and T are the effective reflection coefficient and effective transmission coefficient, respectively. Since d_3 will cancel with that in M_{23}, the value of d_3 in Eq. (11) can be an arbitrary number. Equation (11) represents two equations, so we can obtain unknown R and T.

The metal is a conducting medium (i.e., a high-loss medium with $\sigma \gg \omega\epsilon$ at the MMW band), so the reflectivity of the metal is about equal to 1.0. The stealth material with the metal backplane can be considered as "opaque." Hence, the emissivity is given by the effective reflection coefficient R as[16]

$$e = 1 - |R|^2. \quad (12)$$

The corresponding vertical polarization solution can be obtained by duality, i.e., by replacing E, H, ϵ, μ with H, E, μ, ϵ, respectively.

The brightness temperature received by the MMW radiometer consists of the self-emission brightness temperature from the material and the ambient brightness temperature incident on the material at the reflection angle. The emissivity measurement setup is illustrated in Fig. 2. $\vec{n}$ is the normal vector of the material surface. $T_B(\theta, p)$ and $T_{am}(\theta, p)$ are the measured brightness temperatures of the material and ambient, respectively. $p = v$ or h denotes the vertical or horizontal polarization.

The atmospheric effect can be neglected due to the close measurement range, so $T_B(\theta, p)$ is written as[17]

$$T_B(\theta, p) = e(\theta, p) T_0 + [1 - e(\theta, p)] T_{am}(\theta, p), \quad (13)$$

where θ denotes the incident angle (i.e., the angle between the observation direction and the normal vector of the material surface). T_0 denotes the physical temperature of the material. So the emissivity can be solved as

$$e(\theta, p) = \frac{T_B(\theta, p) - T_{am}(\theta, p)}{T_0 - T_{am}(\theta, p)}. \quad (14)$$

As show in Fig. 2, $T_{am}(\theta, p)$ can be measured independently by manually rotating the radiometer to the dotted line position. Three kinds of stealth materials have been measured in the experiments: these are MSM-R,

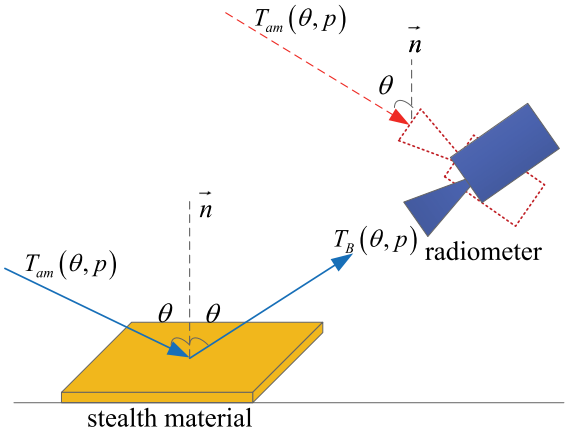

Fig. 2. Schematic of experimental setup. The stealth materials are put on the ground.

BSM-RI and MSM-I. The measurements were conducted at incident angles $\theta = 10°, 20°, 30°, 40°, 50°, 60°$, and 70° by using a 35 GHz radiometer and a 94 GHz radiometer. The 35 GHz radiometer has a 400 MHz bandwidth, 1.0 s integration time, 0.6 K radiometric sensitivity, and 3.7° half-power beam width. The 94 GHz radiometer has a 500 MHz bandwidth, 1.0 s integration time, 0.8 K radiometric sensitivity, and 2.3° half-power beam width. The ambient physical temperature in the experimental site was 298 K.

In the simulations, BSM-RI has RAM (i.e., MSM-R, with 1.0 mm thickness) in the lower layer and infrared stealth material (i.e., MSM-I, with 50 μm thickness) in the surface layer. The material's electromagnetic (EM) parameters are obtained or derived from the published literature[12,13,18,19]. The EM parameters of MSM-I are $\epsilon_1 = 6.47 - i2.176e^{-4}$ and $\mu_1 = 1$ at 35 GHz, and $\epsilon_1 = 6.47 - i5.803e^{-4}$ and $\mu_1 = 1$ at 94 GHz. The EM parameters of MSM-R are $\epsilon_2 = 2.53 - i3.44$ and $\mu_2 = 1.6 - i1.63$ at 35 GHz, and $\epsilon_2 = 3.61 - i2.07$ and $\mu_2 = 1.24 - i0.43$ at 94 GHz.

The radar scattering characteristics of BSM-RI are given first. A High Frequency Structure Simulator (HFSS) is used to simulate the monostatic and biostatic far-field RCS of square the BSM-RI plate, which is based on the finite element method. The electric field direction of the incident plane wave is parallel to the plate edge. Figure 3 shows the 10, 35, and 94 GHz simulation results of the BSM-RI plate with the size of 5 cm × 5 cm. Because the BSM-RI plate has the thickness of 1.05 mm and is treated as a cuboid by the HFSS, the monostatic RCSs do not decrease greatly at the large incident angle.

In our measurements, the EM parameters of stealth materials have not been measured due to the absence of relevant instruments. Fortunately, the measurements are used to study the emission characteristics of stealth materials (not to validate the accuracy of the theoretical model), so the EM parameters of the stealth materials used in the simulations and measurements do not need to be the same. The materials we selected have similar features, as previously mentioned. The stealth wavebands of BSM-RI include the infrared band (3.5–5.5 and 8–14 μm, with infrared emittance <0.1) and radar band (i.e., X, Ka, W, with radar reflectivity < -10 dB).

The theoretical simulations and measured results are both depicted in Figs. 4 and 5. Multiple measurements have been conducted to reduce the measurement errors. The theoretical and measured results indicate that:

(1) The MMW emissivity of MSM-I is less than 0.1 at all incident angles. The thermal emission of MSM-I is low level at the MMW band, as well as at the infrared wave band (emittance <0.1).

(2) The emissivity of MSM-R is always larger than that of BSM-RI at 35 and 94 GHz, except at some particular incident angles (i.e., around the Brewster angle). In other words, the addition of the infrared layer decreases the originally "hot" MMW emission and the reduction is 0.1 to 0.2 at almost all incident angles.

(3) The vertical polarization emissivity of BSM-RI is larger than that of MSM-R when the incident angle is greater than a special angle (corresponding to the intersection position). This special angle is between the Brewster angles of BSM-RI and MSM-R.

The addition of the infrared stealth layer not only influences the emission characteristic of BSM-RI, but also affects the absorption performance of MSM-R. The absorption performance of MSM-R is determined by the

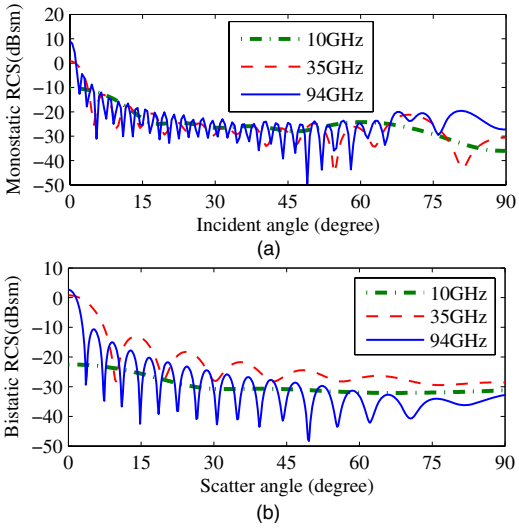

Fig. 3. Monostatic and biostatic RCS of BSM-RI. (a) Monostatic RCS and (b) biostatic RCS under the normal incidence condition.

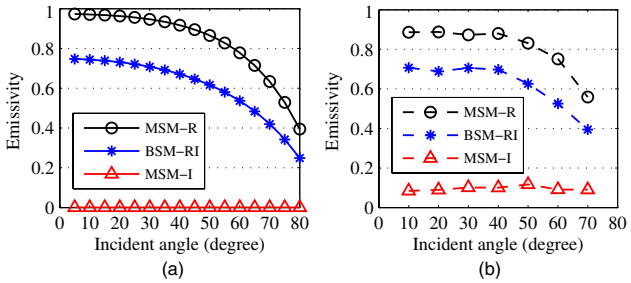

Fig. 4. Emissivity comparison at 35 GHz and horizontal polarization: (a) simulation and (b) measurement.

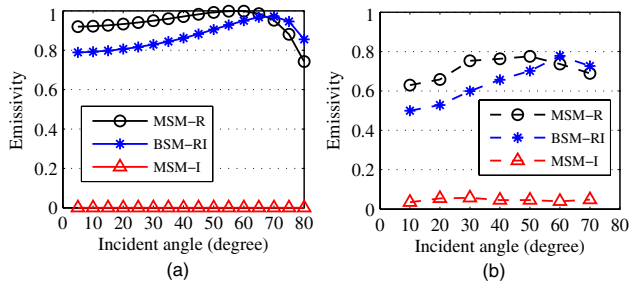

Fig. 5. Emissivity comparison at 94 GHz and vertical polarization: (a) simulation and (b) measurement.

reflection characteristic of the boundary and the absorption performance of the interior material. When an infrared stealth layer is placed on the RAM, the original boundary between the RAM and air will become the new boundary between the RAM and the infrared stealth layer. The change of the boundary can lead to the change of the input impedance of the RAM, which can further influence the boundary reflectivity. Therefore, the absorption performance of MSM-R will also change due to the addition of the infrared stealth layer. Figure 6 depicts the change of the boundary reflectivity at the vertical polarization. Note that the absorption performance of the interior material cannot be affected.

Furthermore, in order to analyze the brightness temperatures in an actual scene, a 94 GHz scanning imaging radiometer system is used for two-dimensional imaging. A high-efficiency Cassegrain antenna (0.3 m diameter) and a direct detection-type MMW detector are mounted at its front end. It features very high detection sensitivity thanks to the integration of high-performance signal processing circuits. The radiometric sensitivity is below 0.8 K, and the half-power beam width of the radiometer antenna is 0.8°. Figure 7 depicts a sketch of the measurement scenes and the corresponding 94 GHz radiometer images. As additional targets, materials ⋆1, ⋆2, and ⋆4 are RAMs and material ⋆3 is a metal plate. In the imaging experiments, the 94 GHz emissivities of materials ⋆1, ⋆2, and ⋆4 are 0.51, 0.43 and 0.88. The physical temperature of the materials is 298 K. All materials are obliquely placed on the ground. The central line of imaging is horizontal and the imaging incident angle is 8°, so the corresponding zenith angle of the reflection direction is 74°. It is known that the 94 GHz sky brightness temperature is about 200 K at the zenith angle of 74° (i.e., $T_{am} \approx 200$ K)[20].

Of special interest are the brightness temperatures of MSM-R, BSM-RI, and MSM-I in Figs. 7(c) and 7(d), all of which show similar regularity to the emissivities. As an example, shown in Fig. 8, the single components of the materials are clearly distinguishable in the horizontal cut of the radiometer images (along the horizontal solid line in Figs. 7(c) and 7(d) in the position of the given stealth materials). According to Eq. (13), T_B increases with the

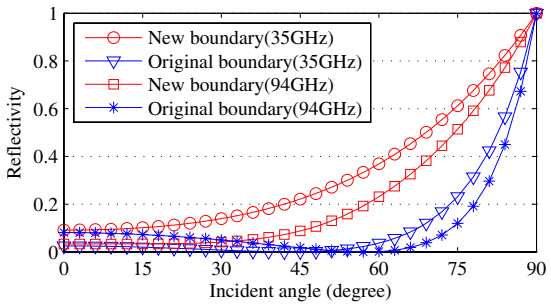

Fig. 6. Change of boundary reflectivity at vertical polarization. Original boundary is the boundary between RAM and air. New boundary is the boundary between RAM and infrared stealth layer.

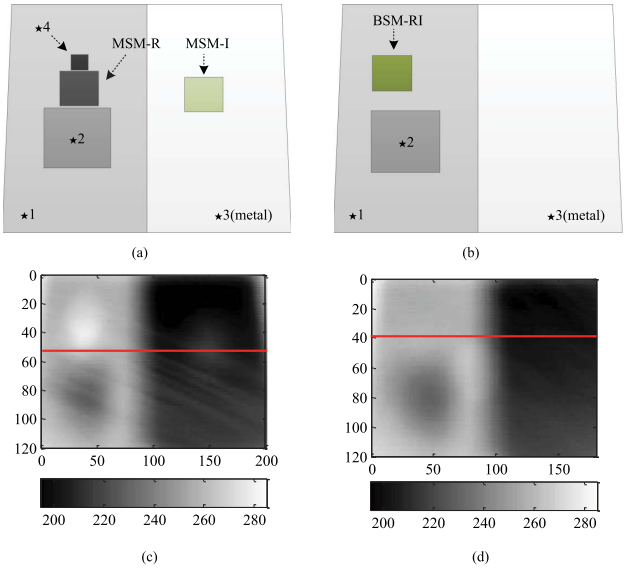

Fig. 7. Sketch of scenes and corresponding 94 GHz radiometer images: (a) materials including MSM-R and MSM-I, (b) materials including BSM-RI, (c) radiometer image of (a), and (d) radiometer image of (b).

increasing MMW emissivity e when $T_0 > T_{am}$. Therefore, the brightness temperature of MSM-R is the largest one and is higher than that of BSM-RI because of the higher emissivity according to Fig. 5(b). Additionally, the brightness temperatures of BSM-RI and material ⋆1 are nearly equal due to having almost the same emissivity. The self-emitted radiation of metal is very small (about zero), so its emission is mainly from the reflected sky background ($T_{am} \approx 200$ K).

Emissivity is a key parameter in measuring the thermal emission ability of substances. According to the theoretical simulations and measured results, the addition of a low-emittance infrared layer leads the MMW emissivity of BSM-RI to reduce 0.1–0.2 at almost every incident angle as compared with MSM-R. A special incident angle (i.e., the Brewster angle) is better for obtaining a high brightness temperature at vertical polarization. Some MMW radiometer images of several stealth materials are obtained in an outdoor environment by using a 94 GHz scanning imaging radiometer system. The imaging results also suggest the MMW emission characteristics of

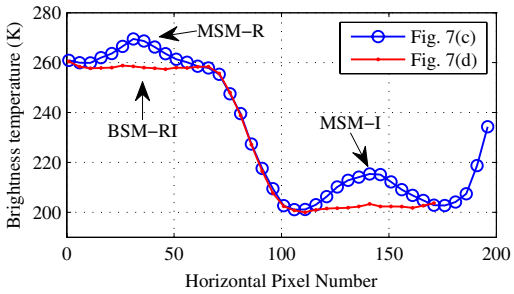

Fig. 8. Horizontal cuts of radiometer images (along the horizontal solid line in Figs. 7(c) and 7(d)).

BSM-RI. The theoretical and measured results partially demonstrate the feasibility of detecting stealth aircraft coated with BSM-RI, as mentioned above. The MMW radiometers may be applied to the area of detecting stealth aircrafts due to the "hot" MMW emission of stealth aircrafts. Meanwhile, many problems, such as real-time imaging technology, limited spatial resolution, and so on remain to be solved before it can be practically applied. In this Letter, we only investigate one particular type of BSM-RI and our results just show the special cases (e.g., isotropic and homogeneous). Other cases in which the material is anisotropic and inhomogeneous will be treated in future work. Additionally, an accurate and professional emissivity measurement system will be developed.

This work was supported partially by the Shanghai Spaceflight Technology Renovation Fund (No. SAST2015088) and the Fundamental Research Funds for the Central Universities (No. HUST2015QN093). The authors would like to thank Prof. Wei Guo for the assistance with the experimental instruments.

References

1. L. Yujiri, M. Shoucri, and P. Moffa, IEEE Microwave Mag. **4**, 39 (2003).
2. S. H. Yueh, W. J. Wilson, S. J. Dinardo, and F. K. Li, IEEE Trans. Geosci. Remote Sens. **37**, 949 (1999).
3. S. Yeom, D.-S. Lee, H. Lee, J.-Y. Son, and V. P. Guschin, Prog. Electromagnet. Res. **115**, 399 (2011).
4. F. Lan, Z. Yang, L. Qi, and Z. Shi, Chin. Opt. Lett. **12**, 040401 (2014).
5. R. Appleby and R. N. Anderton, Proc. IEEE **95**, 1683 (2007).
6. G. Zhang, Z. Zhang, and W. Guo, Int. J. Infrared Millimeter Waves **25**, 929 (2004).
7. L. C. Li, J. Y. Yang, G. L. Cui, Z. M. Jiang, and X. Zheng, J. Infrared Millimeter Terahertz Waves **32**, 102 (2011).
8. Y. Xing, G. Lou, and X. Li, Int. J. Digital Content Technol. Appl. **6**, 10 (2012).
9. W. L. Stewart, IEEE Aerosp. Electron. Syst. Mag. **17**, 11 (2002).
10. K. J. Vinoy and R. M. Jha, *Radar Absorbing Materials- From Theory to Design and Characterization* (Kluwer Academic Publishers, 1996).
11. C. Matzler, *Thermal Microwave Radiation: Applications for Remote Sensing* (The Institution of Engineering and Technology, 2006).
12. L. Liu, R. Gong, D. Huang, Y. Nie, and C. Liu, J. Opt. Soc. Am. A **22**, 2424 (2005).
13. L. Liu, R. Gong, Y. Cheng, F. Zhang, H. He, and D. Huang, Opt. Express **13**, 10382 (2005).
14. D. F. Ren, Y. G. Han, and Y. M. Xuan, Infrared Laser Eng. **41**, 2916 (2012).
15. C. Miao, G. Luo, and X. Li, J. Infrared Millimeter Waves **23**, 221 (2004).
16. F. T. Ulaby, R. K. Moore, and A. K. Fung, *Microwave Remote Sensing: Microwave Remote Sensing Fundamentals and Radiometry* (Addison-Wesley Publishing Company, 1981).
17. Y. Cheng, F. Hu, L. Gui, L. Wu, and L. Lang, IEEE Photon. J. **8**, 5500112 (2016).
18. J. C. M. Garnett, Proc. Royal Soc. London **A203**, 385 (1904).
19. S. K. Andersson, O. Staaf, P. O. Olsson, A. Malmport, and C. G. Ribbing, Opt. Mater. **10**, 85 (1998).
20. X. Lu, Z. Xiao, and J. Xu, Chin. Opt. Lett. **12**, 101201 (2014).